Digest Journal of Nanomaterials and Biostructures Vol. 20, No. 1, January - March 2025, p. 301 – 314

Titanium dioxide nanowires and reduced graphene oxide nanocomposite coated gellan gum film for drug delivery to enhance skin regeneration

J. Yang [a], J. Zhang [b,*], M. Yusoff [c], N. A. Roslan [d], M. H. Razali [d,e]
[a] *Department of Plastic Surgery, AnKang People's Hospital, Ankang, 725000, China*
[b] *Department of Dermatology，Xijing Hospital，Fourth Military Medical University, Xi'an, 710032, China*
[c] *Faculty of Bioengineering and Technology, Universiti Malaysia Kelantan Kampus Jeli, 17600 Jeli, Kelantan, Malaysia*
[d] *Faculty of Science and Marine Environment, Universiti Malaysia Terengganu, 21030 Kuala Nerus, Terengganu, Malaysia*
[e] *Advanced Nanomaterials Research Group, Faculty of Science and Marine Environment, Universiti Malaysia Terengganu, 21030 Kuala Nerus, Terenganu, Malaysia*

This study aimed to fabricate a titanium dioxide nanowires and reduced graphene oxide (TiO_2NWs+RGO) nanocomposite coated with gellan gum film (TiO_2NWs+RGO@GG) for drug delivery to enhance wound healing applications. First, the TiO_2NWs+RGO nanocomposite was synthesised using a single-step hydrothermal method. Subsequently, a comprehensive physicochemical characterization was performed using Fourier transform infrared spectroscopy (FTIR), X-ray diffraction (XRD), scanning electron microscopy (SEM), and thermogravimetry analysis (TGA). The characteristic peak for Ti–O–Ti bonds was observed in the FTIR spectrum between 500 and 850 cm^{-1}. XRD analysis confirmed the presence of reduced graphene oxide (RGO) through the characteristic of aromatic RGO at 2theta of ~25°. Notably, the intensity of the RGO peak was reduced in the TiO_2NWs@RGO composite, indicating successful oxygen functional group reduction. SEM analysis revealed an average diameter of approximately 12.26 ± 1.83 nm for the TiO_2 nanowires within the composite. Antioxidant activity of the synthesised TiO_2NWs+RGO (1:0.5) nanocomposite shows the highest antioxidant activity by DPPH scavenging testing. It was observed that TiO_2NWs+RGO@GG film exhibited good drug release properties, with ibuprofen being released over a duration of 24 hours. The in vitro scratch assays demonstrated that the TiO_2NWs+RGO@GG promotes cell proliferation and migration, facilitating wound closure within 24 hours. Collectively, these findings suggest that the TiO_2NWs+RGO@GG film possess promising properties for wound healing applications.

(Received December 23, 2024; Accepted March 20, 2025)

Keywords: Nanocomposites, Biopolymer, Drug delivery, Wound healing

1. Introduction

Chronic wounds, often arising from diabetes, cardiovascular disease, obesity, and burns, affect millions of individuals globally [1]. Burns alone contribute to over 290,000 fatalities annually, as reported by the World Health Organization (WHO) [2]. Impaired blood flow, excessive water loss (evaporation rate of 2000-2500 m^{-2} per day), and abnormal extracellular matrix deposition can significantly delay wound healing [3]. Maintaining a moist wound environment is crucial during the initial healing phase to protect against external contaminants and bolster the immune response [3, 4]. Prompt and effective treatment is essential to minimize patient exposure to external toxins and promote immunological activity. Consequently, the development of novel wound dressing materials with antibacterial properties, enhanced cell proliferation, and efficient drug delivery is of paramount importance.

---

[*] Corresponding authors: 450643515zje@sina.com
https://doi.org/10.15251/DJNB.2025.201.301

Nanofibers, nanorods, hydrogels, and hydrocolloids are examples of graphene-based nanomaterials that have attracted a lot of interest in wound healing applications because of graphene's advantageous qualities, which include high water vapour transmission rate, hydrophilicity, cytocompatibility, and exceptional mechanical strength [5]. Graphene oxide (GO) exhibits promising differential adhesive and bioactive properties, including the ability to inhibit microbial adhesion [6]. However, the potential cytotoxicity of GO and pure graphene limits their biomedical applications [7]. Reduced graphene oxide (RGO), with its reduced oxygen functional groups, offers a compelling alternative due to its diminished cytotoxicity [8]. Research has shown that RGO stimulates angiogenesis by regulating reactive oxygen species (ROS) levels and promoting good cell adhesion and proliferation [9]. Additionally, RGO has been shown to enhance both collagen synthesis and vascularization, processes vital for wound healing [8, 10]. Chronic wounds pose a significant global health concern, and their management often involves combating bacterial growth. While inorganic nanoparticles exhibit promising antibacterial properties [11], their potential cytotoxicity necessitates careful consideration. Notably, TiO_2 nanoparticles, despite their well-documented biomolecule adsorption capabilities, are generally regarded as inert within biological systems [12]. Seisenbaeva et al. demonstrated that TiO_2 nanoparticle dispersion on burn wounds significantly enhances blood coagulation, a critical step in wound healing [13]. Their study showed a reduction in blood clotting time from 1 minute (untreated serum) to 30 seconds (serum with 1 mg/mL TiO_2 nanoparticles) [13]. Additionally, TiO_2 nanoparticles have been shown by Eldebany et al. to enhance wound healing through the upregulation of vascular endothelial growth factor (VEGF) and transforming growth factor-beta 1 (TGF-β1) signalling pathways [14].

Graphene-based nanocomposites have shown great promise in wound healing applications in recent years because of their improved antibacterial and biocompatible qualities. For example, using cellular acetate, Prakash et al. created GO/TiO_2/curcumin nanofibers, which showed a wound closure rate of $96 \pm 2.23\%$ in just one day [15]. Similarly, studies by Sarayan et al. and Khamrai et al. explored the toxicity of ceramic oxide/ZnO/GO nanocomposites and cellulose/RGO/Ag nanoparticle patches, respectively, demonstrating good cell viability at non-cytotoxic concentrations [16, 17]. Additionally, Shanmugam et al. reported significant wound closure (around 90%) within 72 hours using an RGO/aloe vera gel nanocomposite, highlighting the potential of low-concentration RGO-based materials for wound healing with minimal cytotoxicity [18]. RGO and TiO_2 nanoparticles work together to produce reactive oxygen species (ROS) like OH^- and O_2^-, which further enhances the antibacterial activity of these nanocomposites [19–21].

The use of TiO_2 and RGO nanocomposite films in drug delivery systems holds significant promise for promoting skin regeneration [22]. This approach capitalizes on the unique properties of both materials. The high surface area, mechanical strength, and electrical conductivity of RGO improve the overall performance of the nanocomposite, while the photocatalytic activity and biocompatibility of TiO_2 make it an appropriate drug carrier. [23]. The TiO_2 and RGO nanocomposites can be designed to load various therapeutic agents for wound healing and infection prevention [24]. A critical aspect of this system is the controlled release of drugs and a deeper understanding of drug loading and release mechanisms is crucial for further development. This allows for targeted and sustained delivery, minimizing systemic side effects and maximizing local therapeutic effects [25-27]. Thus, the ultimate goal is to create a robust, effective, and safe drug delivery system that significantly improves skin regeneration and patient outcomes. This study focuses on fabricating TiO_2 nanowires and reduced graphene oxide nanocomposite coated with a gellan gum biopolymers film for efficient drug delivery and enhanced wound healing. Prior to coating, the TiO_2NWs/RGO nanocomposite was synthesized and characterized to investigate its physiochemical properties.

2. Materials and methods

2.1. Materials

Titanium dioxide, sodium hydroxide, sulphuric acid, graphite, sodium nitrate, potassium permanganate, hydrogen peroxide, phosphate buffer, commercial gellan gum were purchased from Sigma-Aldrich. Materials were analytical grade and used exactly as it was delivered.

2.2. Preparation of TiO_2 nanowires

One gram of TiO_2 was added to 100 mL of 10M NaOH aqueous solution. The mixture was then agitated for thirty minutes using a magnetic stirrer. The suspension solution that was produced was then put into Teflon-lined autoclave reactor and heated at 160˚C in the furnace for 10 hours. After the reaction was finished, the white precipitate was cleaned with 0.1M HCl and then deionised water. Deionised water and ethanol were used for further washing. The white precipitate was then filtered and dried for 24 hours at 80˚C in oven. Finally, the synthesised TiO_2 was annealed for 2 hours at 500˚C.

2.3. Synthesis of reduced graphene oxide

A modified version of Hummer's approach was used to prepare GO. In a standard synthesis, 23 ml of H_2SO_4 was mixed quickly while 1.5 g of $NaNO_3$ and 3 g of graphite powder were added. After half an hour, 4 g of KMnO4 was progressively added to the mixture. Don't let the solution get above 10 oC. The combination solution was then put in a water bath set at 35±5°C and agitated constantly for half an hour. The combination solution was then diluted and heated to 98°C by adding 46 millilitres of deionised water. After diluting the combined solution once more with 140 mL of deionised water, it was agitated for half an hour. In order to halt the reaction, 10 mL of H_2O_2 were added to the mixed solution. The mixed solution was then centrifuged again using deionised water after being cleaned with 5% HCl. Overnight, the product was dried in an oven at 60 ºC. As a GO, a dark brown precipitate is formed, and it is then heated to 500 ºC for two hours in a furnace to produce reduced graphene oxide (RGO) film.

2.4. Synthesize of TiO_2NWs and RGO nanocomposites

1.0 gram of TiO_2 nanowires (TiO_2NWs) was dispersed in 50 mL of deionized water using ultrasonication for 30 minutes. The dispersed TiO_2NWs were then drop-cast onto a separate dispersion containing 0.05 g of RGO in 50 mL of deionized water. The combined mixture was subsequently sonicated for 3 hours to facilitate interaction between the components. The resulting suspension was centrifuged at 4000 rpm for 30 minutes to collect the precipitate. After repeatedly washing the collected precipitate with deionised water to get rid of any remaining contaminants, it was dried for 12 hours at 50 °C. Similar procedures were repeated to prepare different nanocomposite by increasing the mass of RGO to 0.5, 1, and 1,5 g, respectively.

2.5. Preparation of TiO_2NWs/RGO@GG nanocomposites film

A100 mL of distilled water containing 0.5 g of glycerol as a plasticiser were mixed with 1g of gellan gum (GG). The mixture was agitated at 1000 rpm for an hour in order to prevent local gelation. After that, the mixture was mixed and heated to 70 °C. The mixture was then crosslinked by adding 5 ml of a 0.5% w/w $CaCl_2$ solution dropwise at a rate of 1 mL/min. The mixture was agitated for another half hour after the $CaCl_2$ solution was added. Subsequently, 0.1 g of the homogeneously dispersed synthetic TiO_2NWs/RGO composite were added to the GG polymer matrix. The blend was thereafter placed onto 9 cm-diameter petri dishes and dried at 40 °C for a full day to produce a film. The TiO_2NWs/RGO@GG film was washed and allowed to air dry for at least 24 hours at room temperature.

2.6. Sample characterization

The sample was distributed in potassium bromide (KBr) before FTIR spectra were taken using a Niconet 5700 FTIR spectrometer. Analysis was conducted between 400 and 4000 cm^{-1} wavenumbers. A Bruker D8 Advance X-ray diffractometer (Bruker AXS, Germany) was used to scan at a speed of 0.2°/s from 10 to 90° of 2θ in order to obtain XRD patterns, which were used to study the crystal structure. Using JEOL JSM 6360LA scanning electron microscopy (SEM) operating at 10 kV, the surface morphology of the catalyst was ascertained. The Mettler Toledo thermal analysis equipment TGA/DSC 1 was used to conduct thermogravimetric analyses (TGA) with heating temperatures ranging from 20 ºC to 700 ºC in order to investigate the weight loss (%) and thermal stability.

2.7. Antioxidant activity of TiO_2NWs+RGO@GG nanocomposites

DPPH at a concentration of 200 µM was dissolved in anhydrous ethanol. After adding 500 mg of TiO_2NWs/RGO nanocomposites to 3 ml of DPPH solution, the mixture was incubated at 37 °C for an hour. The absorbance of the reaction solution was then measured at 517 nm using a UV-vis spectrophotometer. The effectiveness of free radical scavenging was determined using Equation 1:

$$\text{DPPH scavenging} = \frac{A_0 - A_t}{A_0} \text{ x } 100\ \% \tag{1}$$

where A_0 represents the blank's (DPPH solution) absorption and At represents the sample's (DPPH solution + nanocomposite) absorption. Experiment was repeated using TiO_2NWs/RGO nanocomposites at different weight ratio.

2.8. Drug loading efficiency and capacity of TiO_2NWs+RGO@GG nanocomposite film

The study's drug model, 10 mg/ml ibuprofen solution, was made using a DMSO and ethanol combination. Subsequently, the ibuprofen solution was mixed with TiO_2NWs/RGO(1:0.5)@GG film, and the combination was allowed to settle for 24 hours at room temperature in an incubator shaker set at 100 rpm. Following that, the film encapsulating ibuprofen was separated, and the amount of leftover medication in the supernatant was measured using a spectrophotometer set at 275 nm [28, 29]. Previously, the absorbance (A) at 275 nm was measured to create a standard curve by diluting ibuprofen solutions at 2.0, 4.0, 6.0, 8.0, and 10.0 mg/ml. UV-vis spectroscopy of solutions was performed using a spectrophotometer (Varian, Cary 50) with a wavelength range of 200-800 nm, a data interval of 5 nm, and a scan speed of 24,000 nm/min. A 10 mL quartz cells were employed. Every measurement was made three times. Equations 2 and 3 were used to compute the loading efficiency and loading capacity (drug content), respectively;

$$\text{Loading efficiency (\%)} = \frac{\text{Initial Ibuprofen} - \text{Ibuprofen loss}}{\text{Initial Ibuprofen}} \times 100 \tag{2}$$

$$\text{Loading capacity (\%)} = \frac{\text{W(drug loaded)}}{\text{W(TiO}_2\text{NWs/RGO@GG)}} \times 100 \tag{3}$$

where, W(drug loaded) is the weight of ibuprofen loaded, and W(TiO_2NWs/RGO(1:0.5)@GG is the weight of TiO_2NWs+RGO(1:0.5)@GG.

2.9. In vitro drug release

After being submerged in 10 ml of aliquots of 0.1 M phosphate buffer (pH 7.4), the drug-encapsulated TiO_2NWs/RGO(1:0.5)@GG film was incubated for 24 hours at 37 °C. 3 mL aliquots of the specimen were removed after a predetermined amount of time, and new medium was introduced right away. A UV–vis spectrophotometer set at 275 nm was used to quantitatively assess the amount of drug in each aliquot. The medication release was calculated using equation 4:

$$\text{Drug release \%} = \frac{\text{Amount of drug released at time}}{\text{Initial amount of drug encapsulated in the sample}} \text{ x } 100 \tag{4}$$

2.10. In vitro wound healing studies using a scratch wound assay

3T3 fibroblast cells were cultured for 24 hours in a 24-well plate to produce an 80%–90% confluent cell monolayer. In order to prevent cell growth, the cells were additionally exposed to a serum-free medium containing mitomycin C (5 g/mL) for 12 hours before being thrown out and cleaned. Subsequently, the monolayers were scraped with a micropipette tip to form linear wounds featuring a zone free of cells. After scratching, the wells were thoroughly cleaned in PBS three times in order to eliminate any floating or disintegrating cells. Following the addition of the sterile TiO_2NWs/RGO(1:0.5)@GG film to each well, the mixture was incubated with 5% CO_2 at 37 °C. The untreated monolayer of scratched cells covering the entire media made constituted the control group. The wound closure rate was monitored and photographed using an inverted microscope one day after the scratching.

3. Results and discussions

The FTIR spectra of pure TiO_2NWs, RGO and TiO_2NWs/RGO nanocomposites at different weight ratios are shown in Fig. 1. A single, broad band with a maximum intensity at 498 cm^{-1} can be seen in the spectrum of pure TiO2NWs (Fig. 1a) below 1000 cm^{-1}. This band corresponds to the O-Ti-O stretching vibration of the metal-oxygen bond [30]. In Fig. 1b, pure RGO shows a low-intensity peak around 1600 cm^{-1} attributed to the C=C aromatic stretching vibration in the RGO molecule structure [31]. Additionally, peaks within the 1250-1050 cm^{-1} range indicate the presence of C-O stretching modes, further supporting RGO formation. The C=O carbonyl group of carboxylic acids on the surfaces of the RGO nanosheets is represented by the peak at 1719 cm^{-1}, suggesting partial deoxidation of graphene oxide during RGO synthesis [32]. The C-OH and C-O symmetric stretching vibrations are attributed to the stretching bands at 1385 cm^{-1} and 1049 cm^{-1}, respectively [33]. The peak at 1226 cm^{-1} arises from epoxy C-O vibrations. The absence of prominent peaks related to carbon-oxygen functional groups suggests a high degree of GO reduction. A broad peak observed at 3423 cm^{-1} in both pure RGO and TiO_2NWs/RGO nanocomposite samples (Fig. 1c-1f) corresponds to the O-H stretching vibration of hydroxyl groups likely originating from adsorbed water molecules or ambient moisture. The C=O carbonyl group is attributed to the peak at 1730 cm^{-1}, whereas the unoxidized graphitic domains' C=C stretching vibrations are linked to the single peak at 1630 cm^{-1} [34, 35]. Due to its higher intensity, the C=C peak is readily observed in all hybrid ratios, indicating effective hybridization between TiO_2NWs and RGO [34]. The peak at 1400 cm^{-1} corresponds to the wagging vibration of CH_2 and the bending vibration of O-H. The peaks around 1080 cm^{-1} are assigned to C-O-C stretching vibrations [36]. The stretching vibration of the Ti-O and Ti-C bonds is responsible for the wide band seen in the 400–500 cm^{-1} region. The successful grafting of TiO_2 onto the RGO surface is confirmed by the attenuation of these peaks in hybrid samples, which points to a chemical interaction between TiO_2 and RGO.

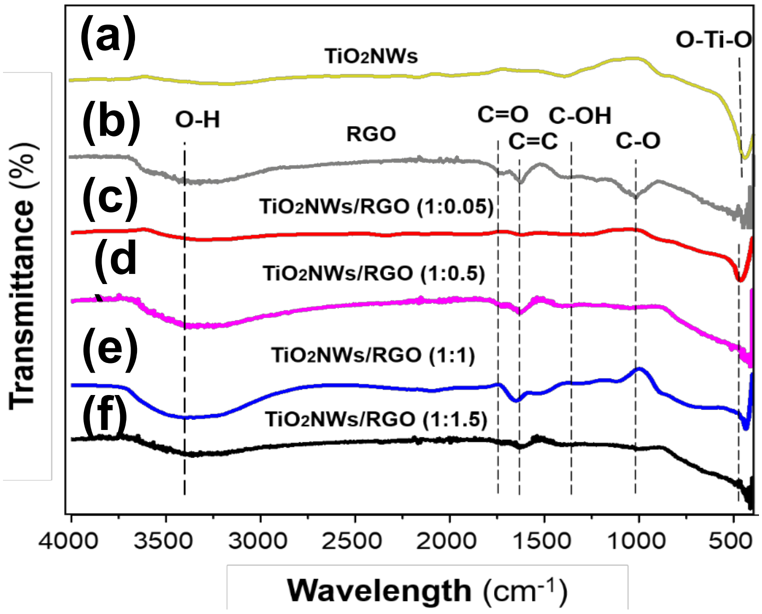

Fig. 1. FTIR spectra of pure TiO_2NWs, RGO and TiO_2NWs/RGO nanocomposites at different weight ratio.

Fig. 2a displays the XRD pattern of the synthesised TiO_2NWs. According to earlier reports [37], the conspicuous peaks at 25.3°, 37.8°, 48.0°, 53.9°, 55.1°, 62.7°, 68.8°, 70.3°, and 75.0° can be indexed to the tetragonal anatase TiO_2 crystal planes (101), (004), (200), (105), (211), (204), (116), (220), and (215). In contrast, the pure RGO sample exhibits a broad and low-intensity reflection peak at approximately 24.1° and 43.9°, corresponding to the (002) and (101) planes of the graphite hexagonal lattice, respectively. These d-spacing values translate to 0.37 nm and 0.28 nm. The observed 2θ values for the RGO sample align well with reported values [38]. The XRD patterns of TiO_2NWs/RGO nanocomposite prepared with varying weight ratios of RGO exhibit differences. Nonetheless, the majority of the diffraction peaks in the hybrid samples correspond to the typical tetragonal anatase TiO_2 XRD pattern (JCPDS No. 71-1187). This implies that the final product's crystal phase is not greatly impacted by the amount of RGO. More precisely, the crystal planes of anatase TiO_2 are displayed by the TiO_2NWs/RGO (1:0.05) hybrid photocatalyst. Similar XRD patterns were obtained for the TiO_2NWs/RGO (1:0.5) sample. The absence of RGO-specific peaks in these two samples is likely due to the low concentration of RGO compared to TiO_2NWs. Notably, no diffraction peaks corresponding to aromatic RGO were observed in the TiO_2NWs/RGO (1:1) and TiO_2NWs/RGO (1:1.5) nanocomposite samples, even at higher RGO concentrations. This phenomenon is likely due to the overlap of the main RGO peak with the (101) peak of anatase TiO_2. Consequently, only one peaks was observed in these samples at 25.5°.

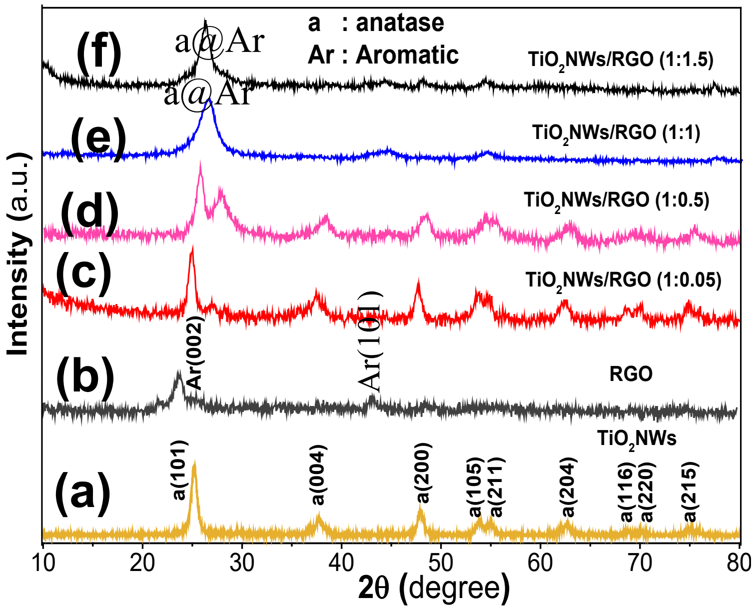

Fig. 2. XRD pattern of pure TiO_2NWs, RGO and TiO_2NWs/RGO nanocomposites at different weight ratio.

Fig. 3 presents the SEM images of pure TiO_2NWs, RGO, and TiO_2NWs/RGO nanocomposites at various weight ratios. Fig. 3a shows the presence of agglomerated TiO_2NWs. This phenomenon is likely due to the calcination process during their preparation, as high temperatures promote particle agglomeration and nanowire bundling [39]. The bundled structure hinders accurate diameter and length measurements. Nevertheless, the synthesized TiO_2NWs were estimated to be around 80 nm in diameter and 200-300 nm length. In contrast, the pristine RGO sample (Fig. 3b) exhibits a sheet-like structure with a smooth surface. These exfoliated sheets are stacked upon each other, forming a layered structure with a thickness less than 100 nm, classifying it as a nanostructured material. The observed sheet-like morphology aligns well with previous reports [40]. This two-dimensional (2D) nanostructure consists of layers with a typical thickness of 1–10 Å and lateral dimensions of tens of microns [41]. Fig. 3c and 3d show that agglomerated TiO_2NWs are attached onto the RGO sheets in the nanocomposite samples, indicating successful loading of TiO_2NWs onto RGO. Well-distributed and decorated TiO_2NWs are observed on the RGO sheets in Figures 3e and 3f, respectively. Enhanced distribution is likely due to the increased layered structure of RGO in the TiO_2NWs/RGO (1:1) and (1:5) samples. Furthermore, increasing the RGO content promotes the distribution of TiO_2NWs on the RGO sheets, leading to more homogeneous TiO_2NWs/RGO nanocomposites. These findings are consistent with previous reports by other researchers [42,43].

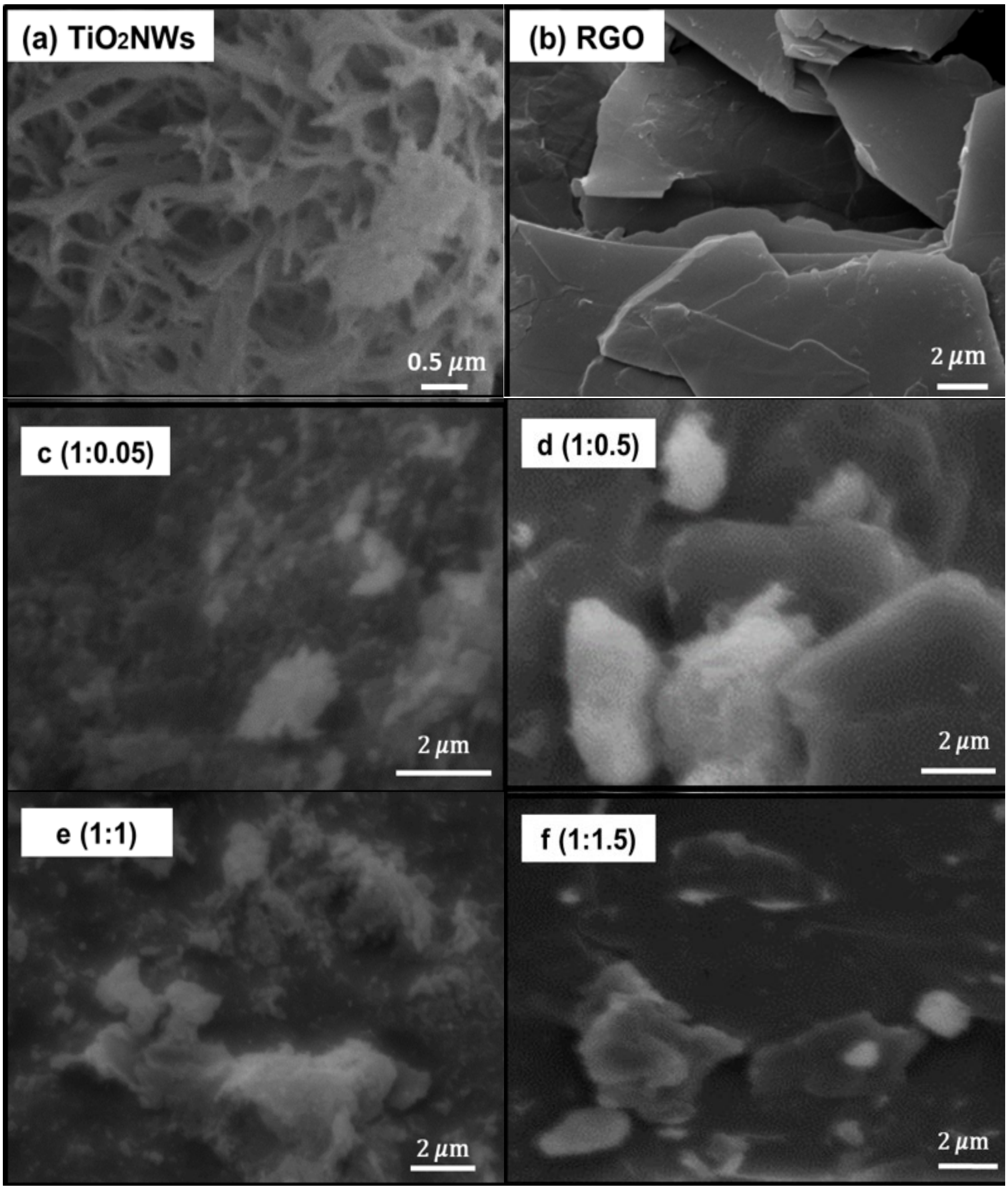

Fig. 3. SEM images of pure TiO_2NWs, RGO and TiO_2NWs/RGO nanocomposite at different weight ratio.

Fig. 4 displays the TGA curves of pure TiO_2NWs, RGO, and TiO_2NWs/RGO nanocomposites at various weight ratios. The pure TiO_2NWs exhibit a single weight loss event around 22% from room temperature to 100 °C, attributed solely to the removal of adsorbed water. As a hydrophilic material, TiO_2 readily undergo hydrolysis and condensation during preparation [44]. In contrast, the TGA curves of RGO and TiO_2NWs/RGO nanocomposites reveal three distinct decomposition stages with corresponding weight losses. The first stage, observed within the range of room temperature to 100 °C, corresponds to the removal of surface-adsorbed water from the samples. The observed weight loss ranges from 4% to 10% for RGO and all studied TiO_2NWs/RGO nanocomposite samples. Notably, the TiO_2NWs/RGO (1:0.05) nanocomposite exhibits the highest initial weight loss due to the presence of a higher amount of hydrophilic TiO_2NWs. Therefore, this nanocomposite sample possessed high thermal stability. The strong interaction between RGO and TiO_2NWs in the TiO_2NWs/RGO (1:0.05) sample is likely responsible for its enhanced thermal stability. Additionally, the low concentration of oxygen groups in the reduced graphene oxide (due to its preparation process) contributes to its resistance to burning and weight loss [45]. The second stage, occurring between 100-600 °C, represents the decomposition of remaining water molecules and functional groups like epoxy and hydroxyl groups within the TiO_2NWs/RGO nanocomposites and pure RGO. The maximum weight loss observed in this stage is approximately 18%. The third and major weight loss stage occurs between 600-850 °C and is attributed to the breakdown of unstable carbon residues within the RGO structure and the pyrolysis of oxygen functionalities leading to the release of carbon dioxide (CO_2) [46]. The weight loss in this stage increases proportionally with the increasing RGO content in the nanocomposites: 10%, 20%, 60%, and 72% for TiO_2NWs/RGO (1:0.05), (1:0.5), (1:1), and (1:1.5), respectively. This trend is consistent with the expectation that a higher RGO content translates to increased CO_2 generation and decreased thermal stability of the hybrid sample. As expected, pure RGO exhibits the highest weight loss (95%), signifying its low thermal stability as a pure carbon structure.

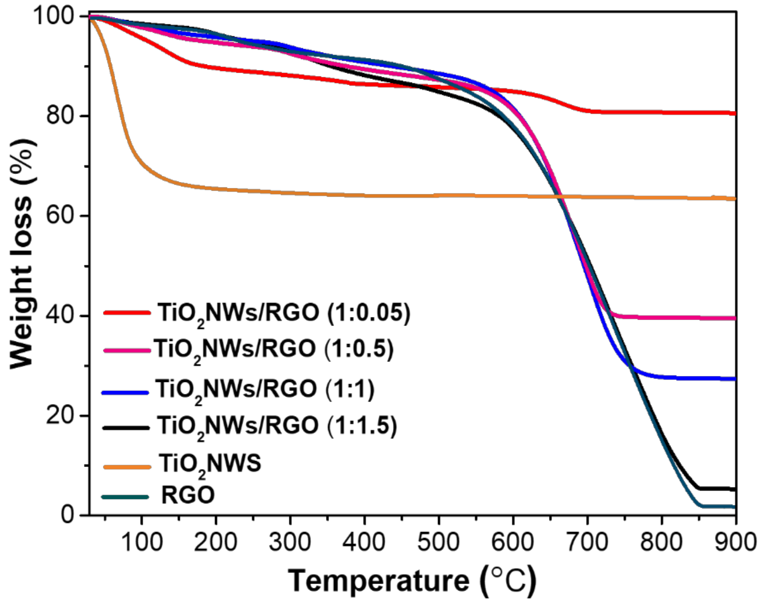

Fig. 4. TGA curves of pure TiO_2NWs, RGO and TiO_2NWs/RGO nanocomposite at different weight ratio.

Fig. 5 illustrates the antioxidant activity of pure TiO_2NWs, RGO, and TiO_2NWs/RGO nanocomposites across different weight ratios. Pure TiO_2NWs exhibited an antioxidant activity of 53.44%. When combined with RGO at weight ratios of 0.1 and 0.5, this activity increased to 81.22% and 92.45%, respectively. This trend demonstrates that higher RGO content significantly enhances the antioxidant properties of the nanocomposites, underscoring the pivotal role of RGO in this enhancement. The underlying mechanism is likely due to the interaction between surface electrons in carbon-TiO_2 pairs and the lone electron pairs on hydroxyl radicals [47]. Prior research has established that the efficacy of antioxidants is closely tied to their electron-donating capabilities [48]. As RGO content rises in the nanocomposites, more surface free electrons are activated, leading to a stronger free radical scavenging effect. However, when the RGO content is increased to 1 and 1.5, the antioxidant activity decreases to 72.84% and 42.82%, respectively. This reduction is attributed to the RGO concentration becoming equal to or exceeding that of TiO_2NWs, resulting in a diminished number of oxygen-containing functional groups available to interact with free radicals [49]. The reduction in these functional groups impairs the material's ability to neutralize free radicals. A similar phenomenon was observed with pure RGO, where antioxidant activity is the lowest with 33.23%.

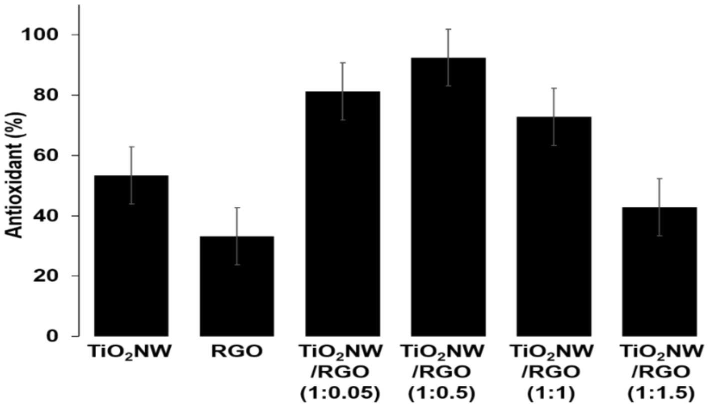

Fig. 5. Antioxidant activity of pure TiO_2NWs, RGO and TiO_2NWs/RGO nanocomposites at different weight ratio.

Based on the antioxidant activity, the TiO_2NWs/RGO (1:0.5) nanocomposite was selected to be loaded with ibuprofen and coated with GG film for drug encapsulation to enhance the wound healing. The encapsulation efficiencies and ibuprofen drug loading within TiO_2NWs/RGO(1:0.05)@GG nanocomposite film was found to be 95.48±0.84% and 78.75±0.75%, respectively. The release profile of ibuprofen was monitored over a period of 24 hours, as depicted in Fig. 6. The release profile of TiO_2NWs/RGO@GG nanocomposite film system exhibited a slow and controlled rate of drug release. About 60% of drug release is shown for the first 3 hours and after 24 hours, the percentage of drug release reached >90%. The release behaviour of drug can be characterized by a two-step process: an initial fast release (burst release) within the first few hours, followed by a relatively slow subsequent release. The application of GG as nanocomposite matrix coating, designed to control and sustain drug release, appears to exhibit a controlled-release profile, suggesting a deliberate design choice for prolonged therapeutic effects. The composition and structure of the GG, along with the physicochemical properties of the drug, play crucial roles in determining release profile [50]. It's plausible that the GG matrix material, with its inherent characteristics, governs the diffusion or degradation processes affecting drug release. Understanding these intricate details is pivotal for tailoring drug delivery systems to achieve desired therapeutic outcomes with precision and efficacy.

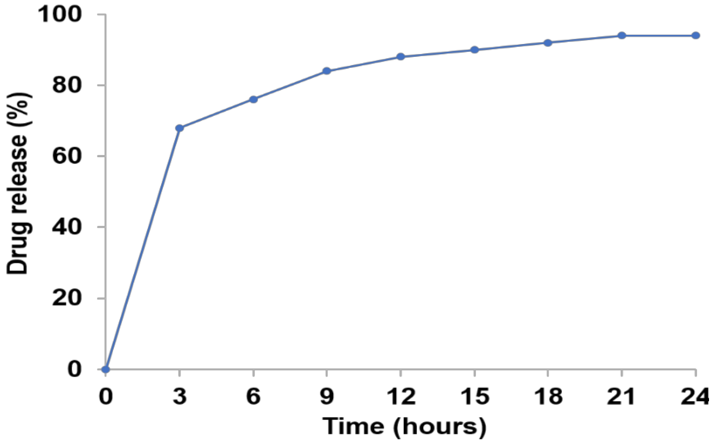

Fig. 6. Drug release profile of ibuprofen by TiO_2NWs/RGO(1:0.5)@GG nanocomposite film.

The in vitro wound healing model via scratch assay was utilized, which is a preferred method for assessing the potential of wound dressing application materials. The finding indicated that the number of cells population that migrated in the TiO_2NWs/RGO(1:0.5)@GG was relatively faster as compared to the control (Fig. 7). It can be observed that the TiO_2NWs/RGO(1:0.5)@GG exhibited a better wound closure function after 24 h, when compared to the control. The TiO_2NWs/RGO (1:0.5)@GG supported a significantly increased cell population, thus demonstrating a pronounced impact on fibroblast migration and wound healing in vitro.

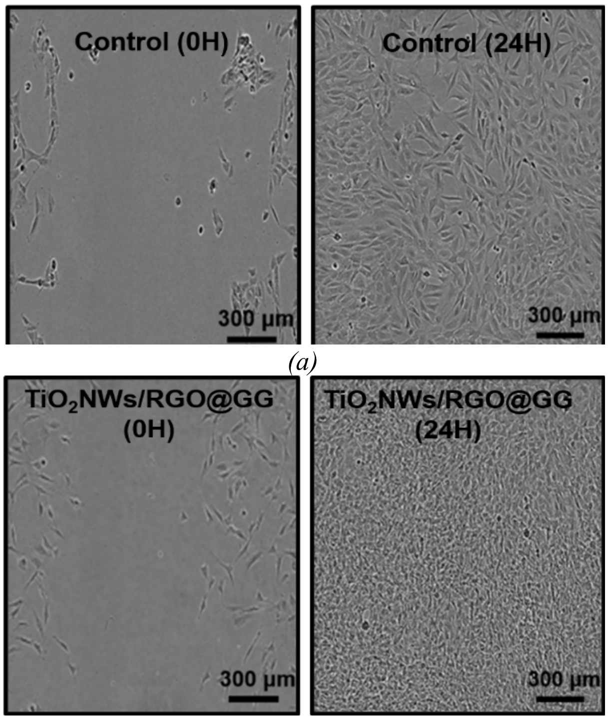

(a)

(b)

Fig. 7. Illustrations of fibroblast cells moving into a scratch area at 0 and 24 hours (a) control sample and in the presence of (b) TiO_2NWs/RGO@GG@ film.

4. Conclusion

In this study, a novel nanocomposite film composed of TiO_2NWs and RGO coated with a gellan gum (GG) matrix, was successfully synthesized and characterized. The TiO_2NWs/RGO(1:0.5) nanocomposite demonstrated excellent antioxidant activity, while TiO_2NWs/RGO(1:0.5)@GG film showed effective drug loading capacity, and controlled drug release properties. The film's ability to facilitate cell proliferation and migration, as evidenced by in vitro scratch assays, indicates its potential to significantly enhance wound healing and skin regeneration. The addition of RGO increased its biocompatibility and thermal stability, making it a viable option for cutting-edge wound care applications.

These findings suggest that the TiO_2NWs/RGO@GG nanocomposite film could offer a robust and efficient platform for drug delivery in biomedical applications, particularly in promoting faster and more effective wound healing. Future work should focus on in vivo studies to further validate the efficacy and safety of this nanocomposite film for clinical applications.

References

[1] Sen, C. K. (2019). Human wounds and its burden: an updated compendium of estimates. Advances in wound care, 8(2), 39-48; https://doi.org/10.1089/wound.2019.0946

[2] Jahromi, M. A. M., Zangabad, P. S., Basri, S. M. M., Zangabad, K. S., Ghamarypour, A., Aref, A. R., Hamblin, M. R. (2018). Nanomedicine and advanced technologies for burns: Preventing infection and facilitating wound healing. Advanced drug delivery reviews, 123, 33-64; https://doi.org/10.1016/j.addr.2017.08.001

[3] Lin, Y., Zhang, Y., Cai, X., He, H., Yang, C., Ban, J., Guo, B. (2024). Design and self-assembly of peptide-copolymer conjugates into nanoparticle hydrogel for wound healing in diabetes. International Journal of Nanomedicine, 2487-2506; https://doi.org/10.2147/IJN.S452915

[4] Olteanu, G., Neacșu, S. M., Joița, F. A., Musuc, A. M., Lupu, E. C., Ioniță-Mîndrican, C. B., & Mititelu, M. (2024). Advancements in Regenerative Hydrogels in Skin Wound Treatment: A Comprehensive Review. International Journal of Molecular Sciences, 25(7), 3849; https://doi.org/10.3390/ijms25073849

[5] Sarkar, P., Ghosal, K., Chakraborty, D., Sarkar, K. (2021). Biocompatibility and biomedical applications of various carbon-based materials. In Handbook of Carbon-Based Nanomaterials (pp. 829-875). Elsevier; https://doi.org/10.1016/B978-0-12-821996-6.00015-4

[6] Cacaci, M., Martini, C., Guarino, C., Torelli, R., Bugli, F., Sanguinetti, M. (2020). Graphene oxide coatings as tools to prevent microbial biofilm formation on medical device. Advances in Microbiology, Infectious Diseases and Public Health: Volume 14, 21-35; https://doi.org/10.1007/5584_2019_434

[7] Gurunathan, S., Kim, J. H. (2016). Synthesis, toxicity, biocompatibility, and biomedical applications of graphene and graphene-related materials. International journal of nanomedicine, 1927-1945; https://doi.org/10.2147/IJN.S105264

[8] Abazari, S., Shamsipur, A., Bakhsheshi-Rad, H. R. (2022). Reduced graphene oxide (RGO) reinforced Mg biocomposites for use as orthopedic applications: Mechanical properties, cytocompatibility and antibacterial activity. Journal of Magnesium and Alloys, 10(12), 3612-3627; https://doi.org/10.1016/j.jma.2021.09.016

[9] Rehman, S. R. U., Augustine, R., Zahid, A. A., Ahmed, R., Tariq, M., Hasan, A. (2019). Reduced graphene oxide incorporated GelMA hydrogel promotes angiogenesis for wound healing applications. International journal of nanomedicine, 9603-9617; https://doi.org/10.2147/IJN.S218120

[10] Thangavel, P., Kannan, R., Ramachandran, B., Moorthy, G., Suguna, L., Muthuvijayan, V. (2018). Development of reduced graphene oxide (rGO)-isabgol nanocomposite dressings for enhanced vascularization and accelerated wound healing in normal and diabetic rats. Journal of colloid and interface science, 517, 251-264; https://doi.org/10.1016/j.jcis.2018.01.110

[11] Jagadeeshan, S., Parsanathan, R. (2019). Nano-metal oxides for antibacterial activity. Advanced nanostructured materials for environmental remediation, 59-90; https://doi.org/10.1007/978-3-030-04477-0_3

[12] Karlsson, H. L., Gustafsson, J., Cronholm, P., Möller, L. (2009). Size-dependent toxicity of metal oxide particles-a comparison between nano-and micrometer size. Toxicology letters, 188(2), 112-118; https://doi.org/10.1016/j.toxlet.2009.03.014

[13] Seisenbaeva, G. A., Fromell, K., Vinogradov, V. V., Terekhov, A. N., Pakhomov, A. V., Nilsson, B., Kessler, V. G. (2017). Dispersion of TiO2 nanoparticles improves burn wound healing and tissue regeneration through specific interaction with blood serum proteins. Scientific reports, 7(1), 15448; https://doi.org/10.1038/s41598-017-15792-w

[14] Eldebany, N., Abd Elkodous, M., Tohamy, H., Abdelwahed, R., El-Kammar, M., Abou-Ahmed, H., Elkhenany, H. (2021). Gelatin loaded titanium dioxide and silver oxide nanoparticles: implication for skin tissue regeneration. Biological Trace Element Research, 199, 3688-3699; https://doi.org/10.1007/s12011-020-02489-x

[15] Prakash, J., Venkataprasanna, K. S., Bharath, G., Banat, F., Niranjan, R., Venkatasubbu, G. D. (2021). In-vitro evaluation of electrospun cellulose acetate nanofiber containing Graphene oxide/TiO2/Curcumin for wound healing application. Colloids and Surfaces A: Physicochemical and Engineering Aspects, 627, 127166; https://doi.org/10.1016/j.colsurfa.2021.127166

[16] Saranya, J., Sreeja, B. S., Arivanandan, M., Bhuvaneswari, K., Sherin, S., Shivani, K. S., Saroja, K. K. (2022). Nanoarchitectonics of cerium oxide/zinc oxide/graphene oxide composites for evaluation of cytotoxicity and apoptotic behavior in HeLa and VERO cell lines. Journal of Inorganic and Organometallic Polymers and Materials, 1-12; https://doi.org/10.1007/s10904-021-02128-5

[17] Khamrai, M., Banerjee, S. L., Paul, S., Ghosh, A. K., Sarkar, P., Kundu, P. P. (2019). A mussel mimetic, bioadhesive, antimicrobial patch based on dopamine-modified bacterial cellulose/rGO/Ag NPs: a green approach toward wound-healing applications. ACS Sustainable Chemistry & Engineering, 7(14), 12083-12097; https://doi.org/10.1021/acssuschemeng.9b01163

[18] Shanmugam, D. K., Madhavan, Y., Manimaran, A., Kaliaraj, G. S., Mohanraj, K. G., Kandhasamy, N., Amirtharaj Mosas, K. K. (2022). Efficacy of graphene-based nanocomposite gels as a promising wound healing biomaterial. Gels, 9(1), 22; https://doi.org/10.3390/gels9010022

[19] Chong, M. C., Winayu, B. N. R., Chu, H. (2024). Advancement of visible light-driven photocatalytic degradation of dimethyl sulfide by Zn doped rGO/TiO2. Applied Surface Science, 648, 159048; https://doi.org/10.1016/j.apsusc.2023.159048

[20] Anwesha, N., Sahu, B. B., Deshmukh, K., Moharana, S. (2024). Graphene Based Antibacterial and Antiviral Functional Materials. In Antibacterial and Antiviral Functional Materials, Volume 2 (pp. 149-184). American Chemical Society; https://doi.org/10.1021/bk-2024-1472.ch005

[21] Zhou, B., Zhao, X., Liu, Y. (2024). The latest research progress on the antibacterial properties of TiO2 nanocomposites. The Journal of The Textile Institute, 1-27; https://doi.org/10.1080/00405000.2024.2349324

[22] Dong, Y., Zheng, Y., Zhang, K., Yao, Y., Wang, L., Li, X., Ding, B. (2020). Electrospun nanofibrous materials for wound healing. Advanced Fiber Materials, 2, 212-227; https://doi.org/10.1007/s42765-020-00034-y

[23] Jahromi, M. A. M., Zangabad, P. S., Basri, S. M. M., Zangabad, K. S., Ghamarypour, A., Aref, A. R., Hamblin, M. R. (2018). Nanomedicine and advanced technologies for burns: Preventing infection and facilitating wound healing. Advanced drug delivery reviews, 123, 33-64; https://doi.org/10.1016/j.addr.2017.08.001

[24] Archana, D., Singh, B. K., Dutta, J., Dutta, P. K. (2013). In vivo evaluation of chitosan-PVP-titanium dioxide nanocomposite as wound dressing material. Carbohydrate polymers, 95(1), 530-539; https://doi.org/10.1016/j.carbpol.2013.03.034

[25] Zhang, H., Wang, G., Yang, H. (2011). Drug delivery systems for differential release in combination therapy. Expert opinion on drug delivery, 8(2), 171-190; https://doi.org/10.1517/17425247.2011.547470

[26] Elumalai, K., Srinivasan, S., Shanmugam, A. (2024). Review of the efficacy of nanoparticle-based drug delivery systems for cancer treatment. Biomedical Technology, 5, 109-122; https://doi.org/10.1016/j.bmt.2023.09.001

[27] Wang, Z., Chen, J., Gao, R., Jiang, L., Zhang, G., Zhao, Y., Shi, Y. (2024). Spatiotemporal manipulation metal-organic frameworks as oral drug delivery systems for precision medicine. Coordination Chemistry Reviews, 502, 215615; https://doi.org/10.1016/j.ccr.2023.215615

[28] Abdallah, N. A., Fathy, M. E., Tolba, M. M., El-Brashy, A. M., Ibrahim, F. A. (2023). Green constant-wavelength concurrent selective fluorescence method for assay of ibuprofen and chlorzoxazone in presence of chlorzoxazone degradation product. Journal of Fluorescence, 33(4), 1661-1671; https://doi.org/10.1007/s10895-023-03175-6

[29] Varga, N., Benkő, M., Sebők, D. Dékány, I., (2014). BSA/polyelectrolyte core-shell nanoparticles for controlled release of encapsulated ibuprofen. Colloids and Surfaces B: Biointerfaces, 123, pp.616-622; https://doi.org/10.1016/j.colsurfb.2014.10.005

[30] Makal, P., Das, D. (2019). Superior photocatalytic dye degradation under visible light by reduced graphene oxide laminated TiO2-B nanowire composite. Journal of Environmental Chemical Engineering, 7(5), 103- 358; https://doi.org/10.1016/j.jece.2019.103358

[31] Maruthamani, D., Divakar, D., Kumarave, M., (2015). Enhanced photocatalytic activity of TiO2 by reduced graphene oxide in mineralization of Rhodamine B dye. Journal of Industrial and Engineering Chemistry, 30, 33-43; https://doi.org/10.1016/j.jiec.2015.04.026

[32] Bashiri, F, Khezri, S.M., Kalantary, R.R., Kakavandi, B., (2020). Enhanced photocatalytic degradation of metronidazole by TiO2 decorated on magnetic reduced graphene oxide: Characterization, optimization and reaction mechanism studies. Journal of Moleculars Liquids, 314, 113- 608; https://doi.org/10.1016/j.molliq.2020.113608

[33] Khan, S. A., Arshad, Z., Shahid, S., Arshad, I., Rizwan, K., Sher, M., Fatima, U. (2019). Synthesis of TiO2/Graphene oxide nanocomposites for their enhanced photocatalytic activity against methylene blue dye and ciprofloxacin. Composites Part B: Engineering, 175, 107120; https://doi.org/10.1016/j.compositesb.2019.107120

[34] Wen, L., Huang, T., Huang, M., Lu, Z., Chen, Q., Meng, Y., Zhou. L. (2020). Secondary reduction of graphene improves the photoelectric properties of TiO2@rGO composites. Ceramics International, 46(7), 9930-9935; https://doi.org/10.1016/j.ceramint.2019.12.087

[35] Venugopal, G., Krishnamoorthy, K., Mohan, R., Kim, S.J. (2012). An investigation of the electrical transport properties of graphene-oxide thin films. Materials Chemistry and Physics, 13(1), 29-33; https://doi.org/10.1016/j.matchemphys.2011.10.040

[36] Wang, C., Cao, M., Wang, P., Ao, Y., Hou, J., & Qian, J. (2014). Preparation of graphene-carbon nanotube-TiO2 composites with enhanced photocatalytic activity for the removal of dye and Cr (VI). 473, 83-89; https://doi.org/10.1016/j.apcata.2013.12.028

[37] Alshammari, A.S., Halim, M.M., Yam, F.K., Kaus N.H.M., (2020). Synthesis of Titanium Dioxide (TiO2)/Reduced Graphene Oxide (rGO) thin film composite by spray pyrolysis technique and its physical properties. Material Science in Semiconducting processing, 116, 105-140; https://doi.org/10.1016/j.mssp.2020.105140

[38] Ebnalwaled, A.A., El-Fadl, A.A., Tuhamy, M.A. (2019). Characterization Studies of Reduced Graphene Oxide/Zinc Oxide Nanocomposites Synthesized by Hydrothermal Method. Journal of Materials and Applications, 8(2), 809; https://doi.org/10.32732/jma.2019.8.2.80

[39] Asiah, M., Mamat, M., Khusaimi, Z., Achoi, M., Abdullah, S., Rusop, M. (2013). Thermal stability and phase transformation of TiO2 nanowires at various temperatures. Microelectronic Engineering, 108, 134-137; https://doi.org/10.1016/j.mee.2013.02.010

[40] Pei, S., Cheng, H. (2012). The reduction of graphene oxide. Carbon, 50(9), 3210-3228; https://doi.org/10.1016/j.carbon.2011.11.010

[41] Chakraborty, P., Das, T., Saha-Dasgupta, T. (2019). A New Trend in 2D Materials Science. Comprehensive Nanoscience and Nanotechnology, 319; https://doi.org/10.1016/B978-0-12-803581-8.10414-X

[42] Hu, J., Li, H., Mohammad, S., Wu, Q., Zhou, Y., Jiao, Q. (2017). Surfactant- assisted hydrothermal synthesis of TiO2/reduced graphene oxide nanocomposites and their photocatalytic performances. Journal Solid State Chemistry, 253, 113-12; https://doi.org/10.1016/j.jssc.2017.05.034

[43] Cheng, G., Xu, F., Xiong, J., Tian, F., Ding, J., Stadler, F.J., Chen, R. (2016). Enhanced

adsorption and photocatalysis capability of generally synthesized TiO2-carbon materials hybrids. Advanced Powder Technology, 27, 1949-1962; https://doi.org/10.1016/j.apt.2016.06.026

[44] Hamad, H.A., Sadik, W.A, El-Latiff, M.M.A., Kashyout, A.B., Fateha, M.Y. (2016). Photocatalytic parameters and kinetic study for degradation of dichlorophenol-indophenol (DCPIP) dye using highly active mesoporous TiO2 nanoparticles. Journal of Environmental Sciences, 43, 26-39; https://doi.org/10.1016/j.jes.2015.05.033

[45] Feng, Y., Wang, B., Li, X., Ye, Y., Ma, J., Liu, C., Zhou, X., Xie, X., (2019). Enhancing thermal oxidation and fire resistance of reduced graphene oxide by phosphorus and nitrogen co-doping: Mechanism and kinetic analysis. Carbon, 146, pp.650-659; https://doi.org/10.1016/j.carbon.2019.01.099

[46] Soltani, T., Lee, B. (2017). Low intensity-ultrasonic irradiation for highly efficient, eco-friendly and fast synthesis of graphene oxide. Ultrasonics Sonochemistry, 38, 693-703; https://doi.org/10.1016/j.ultsonch.2016.08.010

[47] Rehman, G.U., Tahir, M., Goh, P.S., Ismail, A.F., Hafeez, A., Khan, I.U. (2021). Enhancing the photodegradation of phenol using Fe3O4/SiO2 binary nanocomposite mediated by silane agent. Journal of Physics and Chemistry of Solids, 153, 110022; https://doi.org/10.1016/j.jpcs.2021.110022

[48] Wang, C., Cao, M., Wang, P., Ao, Y., Hou, J., Qian, J. (2014). Preparation of graphene-carbon nanotube-TiO2 composites with enhanced photocatalytic activity for the removal of dye and Cr (VI). 473, 83-89; https://doi.org/10.1016/j.apcata.2013.12.028

[49] Wang, W., Wu, Z., Eftekhari, E., Huo, Z., Li, X., Tade, M.O., Yan, C., Yan, Z., Li, C., Li, Q. and Zhao, D., (2018). High performance heterojunction photocatalytic membranes formed by embedding Cu2O and TiO2 nanowires in reduced graphene oxide. Catalysis Science & Technology, 8(6), pp.1704-1711; https://doi.org/10.1039/C8CY00082D

[50] de Oliveira Cardoso, V. M., Evangelista, R. C., Gremião, M. P. D., Cury, B. S. F. (2020). Insights into the impact of cross-linking processes on physicochemical characteristics and mucoadhesive potential of gellan gum/retrograded starch microparticles as a platform for colonic drug release. Journal of Drug Delivery Science and Technology, 55, 101445; https://doi.org/10.1016/j.jddst.2019.101445